Monthly Notices of the ROYAL ASTRONOMICAL SOCIETY
MNRAS **00,** 1 (2020)
Advance Access publication 2020 April 7
doi:10.1093/mnras/staa880

Weak evolution of the mass–metallicity relation at cosmic dawn in the FirstLight simulations

Ivanna Langan,[1,2] Daniel Ceverino[1,3,4,5★] and Kristian Finlator[1,6]

[1] *Cosmic Dawn Center (DAWN) , Denmark*
[2] *Sorbonne Université, faculté des Sciences et Ingénierie, 4 place Jussieu, F-75005 Paris, France*
[3] *Niels Bohr Institute, University of Copenhagen, Lyngbyvej 2, DK-2100 Copenhagen Ø, Denmark*
[4] *Universität Heidelberg, Zentrum für Astronomie, Institut für Theoretische Astrophysik, Albert-Ueberle-Str 2, D-69120 Heidelberg, Germany*
[5] *Departamento de Física Teórica, Universidad Autónoma de Madrid, E-28049 Madrid, Spain*
[6] *New Mexico State University, Las Cruces, NM 88003, USA*

Accepted 2020 March 25. Received 2020 February 27; in original form 2019 October 23

ABSTRACT

Little is known about the mass–metallicity relation (MZR) in galaxies at cosmic dawn. Studying the first appearance of the MZR is one of the keys to understand the formation and evolution of the first galaxies. In order to lay the groundwork for upcoming observational campaigns, we analyse 290 galaxies in haloes spanning $M_{\rm h} = 10^9$–$10^{11}\,{\rm M}_{\odot}$ selected from the FirstLight (FL) cosmological zoom simulations to predict the MZR at $z = 5$–8. Over this interval, the metallicity of FL galaxies with stellar mass $M_* = 10^8\,{\rm M}_{\odot}$ declines by $\leq$0.2 dex. This contrasts with the observed tendency for metallicities to increase at lower redshifts, and reflects weakly evolving or even increasing gas fractions. We assess the use of the $R3$ strong-line diagnostic as a metallicity indicator, finding that it is informative for $12 + \log{(O/H)} < 8$ but saturates to $R3 \approx 3$ at higher metallicities owing to a cancellation between enrichment and spectral softening. None the less, campaigns with *JWST* should be able to detect a clear trend between $R3$ and stellar mass for $M_* > 10^{7.5}\,{\rm M}_{\odot}$. We caution that, at fixed metallicity, galaxies with higher specific star formation show higher $R3$ owing to their more intense radiation fields, indicating a potential for selection biases.

Key words: galaxies: evolution – galaxies: formation – galaxies: high-redshift.

1 INTRODUCTION

Little is known about the abundances of elements heavier than helium in the primeval galaxies of the early Universe. These elements are thought to be produced in the first supernovae explosions (Bromm & Yoshida 2011). Therefore, the generation of heavy elements was quickly linked to star formation processes and galaxy growth, driven by gas inflows, outflows, and merging. In fact, the evolution of the metallicity, the content of heavy elements relative to hydrogen and helium, gives strong insights about these processes (Maiolino & Mannucci 2019).

The galaxy average gas-phase metallicity shows a strong scaling relation with the galaxy stellar mass. The mass–metallicity relation (MZR) has been observed from the local Universe ($z = 0$) to cosmic noon ($z \simeq 3.5$; see Maiolino & Mannucci 2019 for a review of observational efforts). There is a consensus that the MZR evolves at $z < 3.5$ in the sense that, at fixed stellar mass, the metallicity declines with redshift. Does this trend continue to even higher redshifts? There are no observational estimates of metallicities at cosmic dawn ($z \geq 5$) with the exception of GRB afterglows (Berger et al. 2007). Measurements at lower redshifts ($z \leq 3$) are mainly based on strong emission lines, such as [OIII]λ5007. At cosmic dawn, these optical lines are redshifted out of the spectral range of current spectrographs. The James Webb Space Telescope (*JWST*) will soon open a new window into this range, allowing the MZR to traced to much earlier times. Therefore, it is now the best time to make theoretical predictions about the evolution of the MZR at cosmic dawn.

Cosmological simulations have become very advanced tools to study the evolution of the MZR (Finlator & Davé 2008; De Rossi et al. 2017; Torrey et al. 2018; Davé et al. 2019). However, there are only a few cosmological simulations that provide results at cosmic dawn (Barrow et al. 2017; Ceverino, Glover & Klessen 2017; Finlator et al. 2018; Rosdahl et al. 2018; Katz et al. 2019; Ma et al. 2019; Pallottini et al. 2019; Torrey et al. 2019). Most of these works achieve a high resolution using the ‘zoom-in’ technique, which concentrates all computational power on a few select haloes.

The main advantage of zoom simulations over full-box simulations is that they treat the baryon cycle with much more realism. For

★ E-mail: daniel.ceverino@uam.es

© 2020 The Author(s)
Published by Oxford University Press on behalf of the Royal Astronomical Society

example, they model both the emergence of star formation-driven outflows and the small-scale interactions between outflows, the host galaxy's interstellar medium, and the circumgalactic medium more accurately due to their higher resolution and more detailed models of star formation and feedback. As these processes of cooling, star formation, ejection, mixing, and re-accretion are the processes that govern the baryon cycle and the metal enrichment within galaxies, it is important to compare predictions emerging from both simulation techniques.

The traditional drawback to zoom-in simulations is that they do not reveal the ensemble statistical properties of galaxy populations such as the MZR and its scatter. Consequently, most of works focus on the formation of few galaxies. The FirstLight (FL, Paper I Ceverino et al. 2017) data base of ∼300 zoom-in simulations overcomes this limitation. Moreover, FL galaxies agree well with a variety of observations at z = 5–8, such as the UV luminosity function or the stellar mass function (Paper I), the SFR–M_* relation (Paper II, Ceverino, Klessen & Glover 2018) and M_*–Luminosity relations (Paper III, Ceverino, Klessen & Glover 2019). Thus, the FL data base is the ideal laboratory to study the predicted MZR at $z \geq 5$.

This paper has two well-defined goals. After the description of simulations (Section 2), we characterize the MZR at different redshifts at cosmic dawn (Section 3.1) and study its evolution (Section 3.2). Then, we provide metal-sensitive observables (Section 3.3) that can be used in the calibration of future measurements of metallicity at cosmic dawn. Section 4 ends with the summary and discussion.

2 SIMULATIONS

This paper uses a complete mass-selected subsample from the FL data base of simulated galaxies, described fully in Paper I. The subsample consists of 290 haloes with a maximum circular velocity ($V_{\rm max}$) between 50 and 250 km s^{-1}, selected at $z = 5$. The haloes cover a mass range between a few times 10^9 and 10^{11} M$_\odot$. This range excludes more massive and rare haloes with number densities lower than $\sim 3 \times 10^{-4}\,(h^{-1}\,{\rm Mpc})^{-3}$, as well as small haloes in which galaxy formation is extremely inefficient.

The target haloes are initially selected using low-resolution N-body only simulations of two cosmological boxes with sizes 10 and 20 h^{-1}Mpc, assuming WMAP5 cosmology with $\Omega_{\rm m} = 0.27$, $\Omega_{\rm b} = 0.045$, $h = 0.7$, and $\sigma_8 = 0.82$ (Komatsu et al. 2009). We select all distinct haloes with $V_{\rm max}$ at $z = 5$ greater than a specified threshold, log $V_{\rm cut} = 1.7$ in the 10 h^{-1}Mpc box and log $V_{\rm cut} = 2.0$ in the 20 h^{-1}Mpc box. Initial conditions for the selected haloes with much higher resolution are then generated using a standard zoom-in technique (Klypin, Trujillo-Gomez & Primack 2011). The DM particle mass resolution is $m_{\rm DM} = 10^4$ M$_\odot$. The minimum mass of star particles is 100 M$_\odot$. The maximum spatial resolution is always between 8.7 and 17 proper pc (a comoving resolution of 109 pc after $z = 11$).

The simulations are performed with the ART code (Kravtsov, Klypin & Khokhlov 1997; Kravtsov 2003; Ceverino & Klypin 2009; Ceverino et al. 2014, Paper I) that accurately follows the evolution of a gravitating N-body system and Eulerian gas dynamics using an adaptive mesh refinement (AMR) approach. Besides gravity and hydrodynamics, the code incorporates many of the astrophysical processes relevant for galaxy formation. These processes, represented via subgrid physical prescriptions, include gas cooling due to atomic hydrogen and helium, metal and molecular hydrogen cooling, photoionization heating by a constant cosmological UV background with partial self-shielding, star formation, and feedback (thermal + kinetic + radiative), as described in Paper I. The simulations track metals released from SNe-Ia and from SNe-II, using supernovae yields that approximate the results from Woosley & Weaver (1995). These values are given for gas cells and star particles as described in Kravtsov (2003).

We assume that the unresolved nebular region around each star particle shares the same mass ratio of metals produced in SN II explosions as in the star particle (Paper III). The galaxy metallicity is defined as the mass-weighted average nebular metallicity including all star particles younger than 100 Myr. Using the supernovae yields included in the simulation (Woosley & Weaver 1995), our definition of solar metallicity corresponds to $Z_\odot = 0.02$ and $\log(O/H) + 12 = 8.9$. This normalization differs from other simulation works, such as Torrey et al. (2019), which assume a slightly lower value of 8.6. This systematic difference in normalization is comparable to the ∼factor-of-two uncertainties in observational metallicity calibrations (Kewley & Ellison 2008). It does not impact our current study, which focuses on the relative evolution of the MZR at cosmic dawn.

The luminosities of metal-sensitive emission lines are extracted from the publicly available SEDs described in Paper III. In summary, the SEDs of the simulated galaxies are computed using publicly available tables from the Binary Population and Spectral Synthesis (BPASS) model (Eldridge et al. 2017) including nebular emission (Xiao, Stanway & Eldridge 2018). We combine all individual SEDs coming from all star particles within each galaxy. The nebular emission originates in regions around star particles younger than 100 Myr.

As described in Xiao et al. (2018), we compute the line luminosities of a single nebular region around a star particle by assuming a constant nebular density of $n_{\rm H} = 300\,{\rm cm}^{-3}$, because the simulations do not resolve the nebular regions around young stars where most of the nebular light is emitted. This is the value normally used in the literature (Steidel et al. 2016). Denser H II regions, $n_{\rm H} = 1000\,{\rm cm}^{-3}$, give similar results for the SSP metallicities considered in this paper (Xiao et al. 2018). Next, we measure the ionization parameter at the Strömgren radius. The Strömgren radius for each star particle is calculated using the assumed nebular density and the properties of the stellar population. Finally, we use a publicly available grid of Cloudy models to derive the luminosities of the most prominent optical and UV emission lines. More details can be found in Xiao et al. (2018).

Radiative transfer effects and dust attenuation are not included in the analysis. These could affect the rest-frame optical line luminosities of the most massive galaxies, $M_* > 10^8$ M$_\odot$. Paper III has shown that the computed dust-free UV slope (β) is consistent with observations (Bouwens et al. 2014) for galaxies fainter than $M_{\rm UV} \simeq -19$. In other words, available observations are consistent with the assumption that dust obscuration has a minor impact on the luminosity ratios of rest-frame optical lines for most of the FL sample.

3 RESULTS

3.1 The mass–metallicity relation

In Fig. 1, we show that a tight MZR is predicted to exist throughout z = 5–8. Moreover, it evolves very little with redshift. We do not see a change in the slope, as reported by Torrey et al. (2019) at $M_* \simeq 10^9$ M$_\odot$. The shallower slope in FL results from the minimum wind velocity imposed in the recent Illustris model (Pillepich et al. 2018).

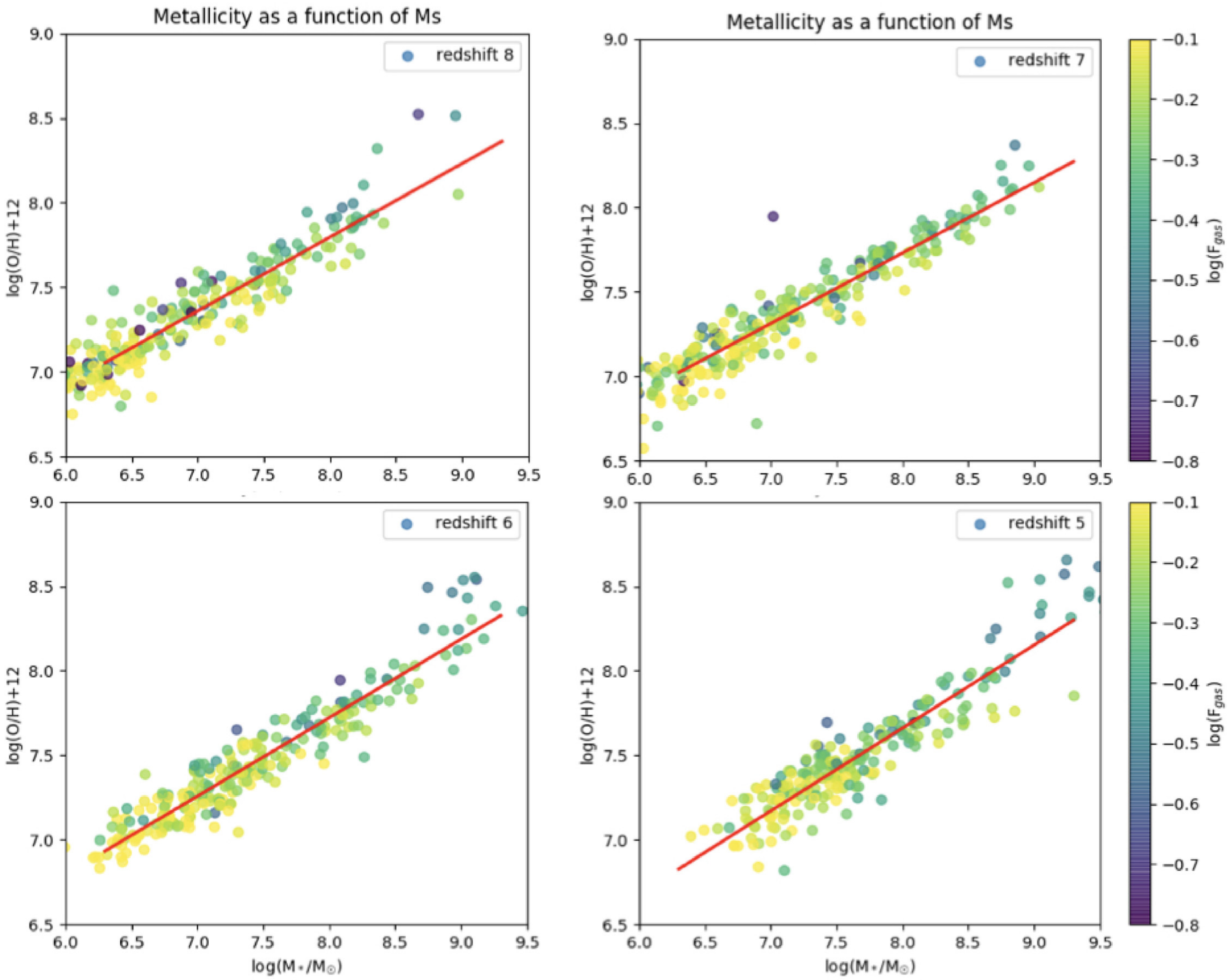

Figure 1. Metallicity as a function of the stellar mass from redshift $z = 5$–8. The colour bar represents the gas fraction. The red lines mark the linear fit. There is weak evolution of this scaling relation at cosmic dawn.

This assumption reduces the mass loading factor (that is, the gas outflow rate in units of SFR) in comparison to what occurs without such a velocity floor (Torrey et al. 2019). A reduced loading factor naturally increases the galaxy metallicity at a fixed stellar mass because more metals are retained in the ISM rather than expelled (Lilly et al. 2013; Finlator 2017).

Observations indicate that the scatter in the MZR correlates with other galaxy properties including gas fraction and SFR (Maiolino & Mannucci 2019). Previous cosmological full-box simulations have reported this correlation at lower redshifts, $z \leq 4$ (De Rossi et al. 2017; Davé et al. 2019; Torrey et al. 2019). In order to explore whether this is expected even at $z \geq 6$, we use colours to indicate the gas fraction $F_{\rm gas}$, defined as $F_{\rm gas} \equiv M_{\rm gas}/(M_{\rm gas} + M_*)$ in Fig. 1. Indeed, it does seem that a residual correlation between Z and $F_{\rm gas}$ contributes significantly to the MZR scatter. For example, galaxies with higher-than-average gas fractions, $F_{\rm gas} \simeq 0.7$, have preferentially lower metallicities, at a fixed stellar mass of 10^8 M$_\odot$. In the same mass bin, galaxies with lower-than-average gas fractions, $F_{\rm gas} \simeq 0.3$, have metallicities higher by 0.2 dex than average. As shown in Paper II, a higher gas fraction correlates with a higher star formation rate for a given mass and redshift. Therefore, the FL simulations predict that the fundamental mass–metallicity relation (Ellison et al. 2008; Maiolino & Mannucci 2019) has already emerged by cosmic dawn.

3.2 Weak evolution of the MZR

Fig. 2 (blue circles) shows the average metallicity and its scatter (vertical error bars) within a narrow mass bin centred at $M_* = 10^8$ M$_\odot$ at different redshifts across cosmic dawn. These average values agree well with the linear fits used in Fig. 1 (yellow diamonds). They show weak evolution of the MZR at these redshifts. In fact, there is even a hint that metallicity declines by ~0.15 dex from $z = 8$–5, although the decline is similar to the intrinsic scatter of the relation.

We can show that this weak evolution is driven by weak evolution in $F_{\rm gas}$ by invoking the *effective yield* (Garnett 2002; Dalcanton 2007). If a galaxy is a closed-box system, then the gas metallicity

$$Z_{\rm g} \equiv M_{\rm metals}/M_{\rm gas} \tag{1}$$

is a function of $F_{\rm gas}$ and the intrinsic stellar yield, $y = 0.02$, which expresses the ratio of the mass of new metals released into the ISM to the mass in long-lived stars. In the more general case where inflows and outflows are permitted, $y_{\rm eff}$ quantifies their net impact on a galaxy's chemical content

$$Z_{\rm g} = -y_{\rm eff}\ \ln(F_{\rm gas}). \tag{2}$$

Under the assumption that the net impact of inflows and outflows is constant throughout our redshift range and stellar mass bin, $y_{\rm eff}$ is

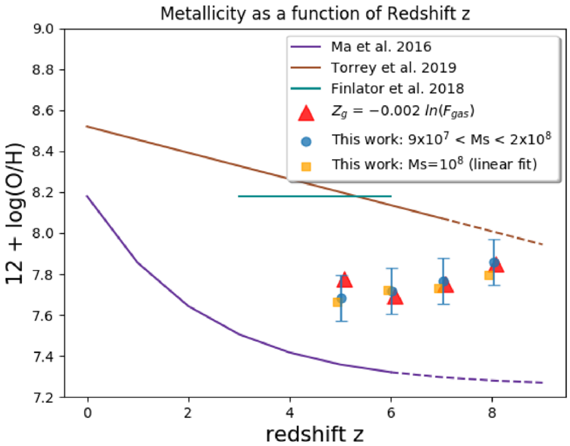

Figure 2. The evolution of metallicity at fixed stellar mass, $M_* = 10^8\ \mathrm{M_\odot}$. Blue circles and yellow squares indicate FL predictions while coloured curves indicate predictions from other simulations (dashed lines indicate an extrapolation in redshift). Red triangles show the predicted evolution if the effective yield is fixed to $y_{\rm eff} = 0.002$ and $F_{\rm gas}(z, M_* = 10^8\ \mathrm{M_\odot})$ is adopted directly from our simulations (Section 3.2). Note that yellow squares and red triangles are offset slightly in redshift for clarity.

constant and the MZR's evolution in time at a fixed stellar mass is driven by evolution in $F_{\rm gas}$. The average gas fractions increase from $F_{\rm gas} \simeq 0.45$ at $z = 8$ to $F_{\rm gas} \simeq 0.55$ at $z = 6$. In order to verify that this suffices to drive the predicted metallicity evolution, we use red triangles in Fig. 1 to plot the quantity $-0.002\ln(F_{\rm gas})$. This model closely tracks the FL simulations throughout $z = 8 \rightarrow 6$, supporting the idea that slowly increasing gas fractions indeed dominate early metallicity evolution within the full simulation. From $z = 6 \rightarrow 5$, the agreement is weaker, although the constant effective yield model still agrees with the simulation to within the simulated scatter. For context, we note that the assumed value $y_{\rm eff} = 0.002$ is similar to the values found in local galaxies of similar mass (Tremonti et al. 2004). The effective yield is 10 times smaller than the intrinsic yield, indicating that the interstellar media of reionization-epoch galaxies were highly dynamical environments characterized by a vigorous interplay between metal-rich outflows and pristine inflows.

The slowly increasing gas fractions that arise in our simulations predict that, prior to $z \simeq 5$, galaxies build up their gas reservoirs because the rate at which star formation and outflows process their ISM lags the gas accretion rate. In this regime, dilution from pristine inflows dominates over enrichment, leading to constant or even slowly decreasing gas-phase metallicities (see also Wu et al. 2019).

As the MZR at $z > 4$ remains unconstrained observationally, we focus on a comparison with predictions from other theoretical models. Ma et al. (2016b) show results up to $z = 6$ and Torrey et al. (2019) extend it to $z = 7$. In order to facilitate comparison with FL predictions, we extrapolate their fitting relations to our range of redshifts. In doing so, we normalize their predictions to the same solar abundance that we assume (see Section 2). Our metallicity values lie in between these predictions. The values are close, within $\sim$0.5 dex. This is encouraging because these simulations use slightly different definitions of metallicity but they claim to reproduce the same observed values at lower redshifts, $z \leq 2$.

However, there are some important differences in the evolution of the MZR with respect to these previous works. In Torrey et al. (2019), we can see that the metallicity strongly decreases with redshift at all times. This evolution is driven by the artificial velocity floor imposed on the outflows, as described above. Indeed, their massive galaxies, $M_* \geq 10^{9.5}\ \mathrm{M_\odot}$, start to show a flattening in their metallicity evolution with redshift at $z \simeq 5$. This is because more massive galaxies have outflows with higher velocities and they are not affected by this velocity floor.

The simulations by Finlator et al. (2018) show no metallicity evolution from $z = 3$–6, roughly consistent with our findings at higher redshifts. Although their wind model is similar to Torrey et al. (2019), it does not include the velocity floor. Most probably, this is why their metallicity does not decrease with redshift as in previous works. This highlights the importance of galactic outflows in the evolution of the metal content in galaxies.

The simulations by Ma et al. (2016a) predict a flattening of the metallicity evolution with increasing redshift, roughly consistent with the weak evolution in FL. However, the predicted metallicities are systematically lower by 0.3 dex. It is likely that the outflows in these simulations are far more efficient in removing metals from small galaxies. Indeed, Agertz et al. (2020) have shown that this model struggles to reproduce the observed plateau of stellar abundances in the faintest dwarfs in the local volume.

These comparisons highlight the importance of metallicity as a sensitive test of feedback models. Two questions motivated by this discussion include. First, when are galaxies predicted to graduate from building up their gas reservoirs to exhausting them? The epoch at which $F_{\rm gas}$ peaks may manifest observationally via a minimum in the MZR normalization. Secondly, how can upcoming measurements of $F_{\rm gas}$ and $Z_{\rm gas}$ be used to identify this transition? Over the next decade, observations of galaxies and their circumgalactic media at cosmic dawn will distinguish between these models, illuminating how the MZR first emerged.

3.3 Metallicity indicators

We now assess the strong rest-frame optical emission line diagnostics that will soon be used to test the predictions in the previous sections. These lines are widely used to infer the metallicities of low-redshift galaxies because they are bright and easily accessible using ground-based measurements. At reionization-epoch redshifts, however, only *JWST* can open up rest-frame optical diagnostics of galaxy evolution.

From the published mock optical spectra of the galaxies in the FL data base (Paper III), we measure the luminosities of [OIII]λ5007, OII ($\equiv$[OII]λ3727 + [OII]λ3729), and Hβ. From these fluxes, we compute the metallicity-sensitive *R2* and *R3* indices following Maiolino & Mannucci (2019). As oxygen is the most abundant heavy element, we can compare them with the intrinsic gas-phase metallicities discussed in the previous section. In practice, we have found that the contribution of *R2* to *R23* (which is the sum or *R2* and *R3*) is very small. We therefore focus on *R3*, with the understanding that qualitative results apply also to *R23*.

In Fig. 3, we plot *R3* versus the galaxy metallicity. For $12 + \log(O/H) < 8$, *R3* increases strongly with gas-phase metallicity. At higher metallicities, it saturates. This behaviour reflects a competition between enrichment and ionization. For $12 + \log(O/H) < 8$, a slight increase in metallicity boosts the oxygen abundance more significantly than it softens the radiation field, yielding an overall increase to *R3*. At higher metallicities, the two effects largely cancel. As a result, *R3* is a useful probe of metallicity only at low metallicities.

The scatter of this relation is mostly driven by the sSFR (sSFR $\equiv$ SFR/M_*), which correlates with the ionization parameter (Paper III). At a given metallicity, galaxies with higher sSFR have

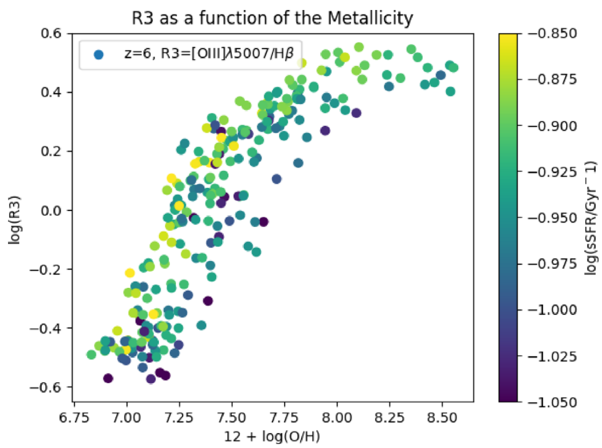

Figure 3. *R3* as a function of the metallicity at redshift $z = 6$. The colour bar represents sSFR. After a maximum value at around $Z = 0.1\,Z_\odot$, *R3* strongly decreases at lower metallicities. For a given metallicity bin, *R3* increases with sSFR.

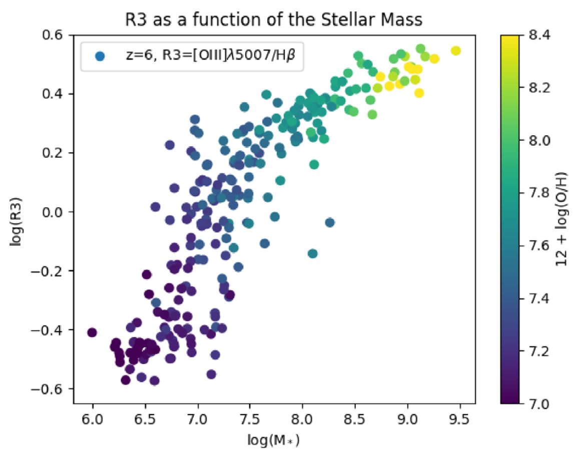

Figure 4. *R3* as a function of the stellar mass at redshift $z = 6$. The colour bar represents the metallicity in oxygen units. There is drop in *R3* which corresponds to a metallicity around 7.5 and a stellar mass around $10^{7.5}\,M_\odot$.

systematically higher *R3* values. These galaxies are usually brighter and easier to observe. This could introduce a bias towards high *R3* values in the observations of the faintest galaxies.

In Fig. 4, we plot *R3* versus the galaxy stellar mass. Here, we see a clear trend of increasing *R3* with mass. The trend is mostly driven by the galaxy metallicity. There is a drop in *R3* at $M_* \simeq 10^7\,M_\odot$, driven by the low oxygen abundance, as in Fig. 3. JWST will only just be capable of observing such low-mass galaxies in blank fields. Ultradeep fields with a limiting magnitude of $m = 31$ in the rest-frame UV would be mass completed for $M_* \geq 10^{7.5}\,M_\odot$ at $z = 6$ (Paper III). JWST samples of smaller galaxies will be biased towards higher sSFRs, which could prevent detection of the predicted drop in *R3* towards lower masses.

4 DISCUSSION AND SUMMARY

We have used the FL data base of cosmological zoom-in simulations to study the mass–metallicity relation at cosmic dawn. The main results can be summarized as follows:

(i) The MZR, well-known at low redshifts, is predicted to exist at high redshifts ($z = 5$–8).

(ii) The scatter of the MZR is driven by the gas fraction.

(iii) The average metallicity at a fixed stellar mass evolves weakly – and may even decrease – during the interval $z = 8 \rightarrow 5$. This evolution is driven by slowly increasing gas fractions during the epoch of gas reservoir buildup.

(iv) The emission lines ratios *R3* and *R23* correlate relatively well with both metallicity and stellar mass. However, a secondary dependence on sSFR could introduce observational biases, particularly in samples that are not mass selected.

(v) There is an abrupt decrease of *R3* at low metallicities and low masses driven by low metal abundances.

Galaxy spectra from JWST will open a new window to the rest-frame optical at cosmic dawn (Álvarez-Márquez et al. 2019). New measurements of emission lines ratios at these high redshifts will give us the first direct determination of galaxy metallicities in the early Universe. However, a lot of work on calibration of these metal tracers will be needed. This work provides the first attempt to look at these metallicity tracers from cosmological simulations. Still, systematic uncertainties remain. The choice of different line-emission models could affect the calibration. The choice of stellar evolution model (in our case, BPASS) is another source of uncertainty. Future works will address the systematics associated with these decisions and the effect in the overall normalization. However, the reported evolutionary trends are robust to choices that only affect the MZR's normalization.

Other caveats are intrinsically related to the FL simulations. First, they do not follow individual elements, like oxygen, carbon, or nitrogen. Therefore, we rely on published supernovae yields to estimate the oxygen abundances from the total amount of metals produced in core-collapsed supernovae. This is a good assumption for oxygen because it is mostly generated in these supernovae. However, other important elements, like carbon or nitrogen, have also secondary production channels, like AGB winds, which are not included. In addition, radiative transfer effects are only considered at post-processing on unresolved scales. The structure and dynamics of nebular regions on very small scales may also affect O III luminosities (Pellegrini et al. 2019). Dust is also not included, although its effect on *R3* is small. Finally, bigger cosmological volumes will be needed to address the metal content in more massive galaxies and/or higher redshifts.

There is still plenty of exciting work to do, things to try and to understand, with respect to the mechanisms of metal production in the early Universe, or more precisely in primeval galaxies. Future works include following the metallicity content of galaxies in the same mass range at $z = 5$–8 by computing the 3D metal distributions in time intervals of 10 Myr. As a second step, we will follow the evolution of $M_{\rm metals}$ and $M_{\rm gas}$ for different galaxies at similar masses but different redshifts. We will check if their evolution could explain the mild increase of metallicity we get with redshift. These follow-up works will get new insights about the origin of the elements in the early Universe.

ACKNOWLEDGEMENTS

We thank Xiangcheng Ma for fruitful discussions. The Cosmic Dawn Center is funded by the Danish National Research Foundation. The FirstLight simulations were performed at Leibniz Supercomputing Centre and bwHPC. DC is a Ramon y Cajal researcher.

REFERENCES

Agertz O. et al., 2020, MNRAS, 491, 1656
Álvarez-Márquez J. et al., 2019, A&A, 629, A9
Barrow K. S. S., Wise J. H., Norman M. L., O'Shea B. W., Xu H., 2017, MNRAS, 469, 4863
Berger E. et al., 2007, ApJ, 665, 102
Bouwens R. J. et al., 2014, ApJ, 793, 115
Bromm V., Yoshida N., 2011, ARA&A, 49, 373
Ceverino D., Klypin A., 2009, ApJ, 695, 292
Ceverino D., Klypin A., Klimek E. S., Trujillo-Gomez S., Churchill C. W., Primack J., Dekel A., 2014, MNRAS, 442, 1545
Ceverino D., Glover S. C. O., Klessen R. S., 2017, MNRAS, 470, 2791
Ceverino D., Klessen R. S., Glover S. C. O., 2018, MNRAS, 480, 4842
Ceverino D., Klessen R. S., Glover S. C. O., 2019, MNRAS, 484, 1366
Dalcanton J. J., 2007, ApJ, 658, 941
Davé R., Anglés-Alcázar D., Narayanan D., Li Q., Rafieferantsoa M. H., Appleby S., 2019, MNRAS, 486, 2827
De Rossi M. E., Bower R. G., Font A. S., Schaye J., Theuns T., 2017, MNRAS, 472, 3354
Eldridge J. J., Stanway E. R., Xiao L., McClelland L. A. S., Taylor G., Ng M., Greis S. M. L., Bray J. C., 2017, Publ. Astron. Soc. Aust., 34, e058
Ellison S. L., Patton D. R., Simard L., McConnachie A. W., 2008, ApJ, 672, L107
Finlator K., 2017, in Fox A., Davé R., eds, Astrophysics and Space Science Library, Vol. 430, Gas Accretion on to Galaxies. Springer-Verlag, Berlin, p. 221
Finlator K., Davé R., 2008, MNRAS, 385, 2181
Finlator K., Keating L., Oppenheimer B. D., Davé R., Zackrisson E., 2018, MNRAS, 480, 2628
Garnett D. R., 2002, ApJ, 581, 1019
Katz H. et al., 2019, MNRAS, 487, 5902
Kewley L. J., Ellison S. L., 2008, ApJ, 681, 1183
Klypin A. A., Trujillo-Gomez S., Primack J., 2011, ApJ, 740, 102
Komatsu E. et al., 2009, ApJS, 180, 330
Kravtsov A. V., 2003, ApJ, 590, L1
Kravtsov A. V., Klypin A. A., Khokhlov A. M., 1997, ApJS, 111, 73
Lilly S. J., Carollo C. M., Pipino A., Renzini A., Peng Y., 2013, ApJ, 772, 119
Maiolino R., Mannucci F., 2019, A&AR, 27, 3
Ma X., Hopkins P. F., Faucher-Giguère C.-A., Zolman N., Muratov A. L., Kereš D., Quataert E., 2016a, MNRAS, 456, 2140
Ma X., Hopkins P. F., Kasen D., Quataert E., Faucher-Giguère C.-A., Kereš D., Murray N., Strom A., 2016b, MNRAS, 459, 3614
Ma X. et al., 2019, MNRAS, 487, 1844
Pallottini A. et al., 2019, MNRAS, 487, 1689
Pellegrini E. W., Reissl S., Rahner D., Klessen R. S., Glover S. C. O., Pakmor R., Herrera-Camus R., Grand R. J. J., 2019, preprint (arXiv:1905.04158)
Pillepich A. et al., 2018, MNRAS, 475, 648
Rosdahl J. et al., 2018, MNRAS, 479, 994
Steidel C. C., Strom A. L., Pettini M., Rudie G. C., Reddy N. A., Trainor R. F., 2016, ApJ, 826, 159
Torrey P. et al., 2018, MNRAS, 477, L16
Torrey P. et al., 2019, MNRAS, 484, 5587
Tremonti C. A. et al., 2004, ApJ, 613, 898
Woosley S. E., Weaver T. A., 1995, ApJS, 101, 181
Wu X., Davé R., Tacchella S., Lotz J., 2019, preprint (arXiv:1911.06330)
Xiao L., Stanway E. R., Eldridge J. J., 2018, MNRAS, 477, 904

This paper has been typeset from a TEX/LATEX file prepared by the author.

List of astronomical key words (Updated on 2020 January)

This list is common to *Monthly Notices of the Royal Astronomical Society, Astronomy and Astrophysics*, and *The Astrophysical Journal*. In order to ease the search, the key words are subdivided into broad categories. No more than *six* subcategories altogether should be listed for a paper.

The subcategories in boldface containing the word 'individual' are intended for use with specific astronomical objects; these should never be used alone, but always in combination with the most common names for the astronomical objects in question. Note that each object counts as one subcategory within the allowed limit of six.

The parts of the key words in italics are for reference only and should be omitted when the keywords are entered on the manuscript.

General
editorials, notices
errata, addenda
extraterrestrial intelligence
history and philosophy of astronomy
miscellaneous
obituaries, biographies
publications, bibliography
sociology of astronomy
standards

Physical data and processes
acceleration of particles
accretion, accretion discs
asteroseismology
astrobiology
astrochemistry
astroparticle physics
atomic data
atomic processes
black hole physics
chaos
conduction
convection
dense matter
diffusion
dynamo
elementary particles
equation of state
gravitation
gravitational lensing: micro
gravitational lensing: strong
gravitational lensing: weak
gravitational waves
hydrodynamics
instabilities
line: formation
line: identification
line: profiles
magnetic fields
magnetic reconnection
(magnetohydrodynamics) MHD
masers
molecular data
molecular processes
neutrinos
nuclear reactions, nucleosynthesis, abundances
opacity
plasmas
polarization
radiation: dynamics
radiation mechanisms:general
radiation mechanisms: non-thermal
radiation mechanisms: thermal
radiative transfer
relativistic processes
scattering
shock waves
solid state: refractory
solid state: volatile
turbulence
waves

Astronomical instrumentation, methods and techniques
atmospheric effects
balloons
instrumentation: adaptive optics
instrumentation: detectors
instrumentation: high angular resolution
instrumentation: interferometers
instrumentation: miscellaneous
instrumentation: photometers
instrumentation: polarimeters
instrumentation: spectrographs
light pollution
methods: analytical
methods: data analysis
methods: laboratory: atomic
methods: laboratory: molecular
methods: laboratory: solid state
methods: miscellaneous
methods: numerical
methods: observational
methods: statistical
site testing
space vehicles
space vehicles: instruments
techniques: high angular resolution
techniques: image processing
techniques: imaging spectroscopy
techniques: interferometric
techniques: miscellaneous
techniques: photometric
techniques: polarimetric
techniques: radar astronomy
techniques: radial velocities
techniques: spectroscopic
telescopes

Astronomical data bases
astronomical data bases: miscellaneous
atlases
catalogues
surveys
virtual observatory tools

Software
software: data analysis
software: development
software: documentation
software: public release
software: simulations

Astrometry and celestial mechanics
astrometry
celestial mechanics
eclipses
ephemerides
occultations
parallaxes
proper motions
reference systems
time

The Sun
Sun: abundances
Sun: activity
Sun: atmosphere
Sun: chromosphere
Sun: corona
Sun: coronal mass ejections (CMEs)
Sun: evolution
Sun: faculae, plages
Sun: filaments, prominences
Sun: flares
Sun: fundamental parameters
Sun: general
Sun: granulation
Sun: helioseismology
Sun: heliosphere
Sun: infrared
Sun: interior
Sun: magnetic fields
Sun: oscillations
Sun: particle emission
Sun: photosphere
Sun: radio radiation
Sun: rotation
(Sun:) solar–terrestrial relations
(Sun:) solar wind
(Sun:) sunspots
Sun: transition region
Sun: UV radiation
Sun: X-rays, gamma-rays

Planetary systems
comets: general

comets: individual: . . .
Earth
interplanetary medium
Kuiper belt: general

Kuiper belt objects: individual: . . .
meteorites, meteors, meteoroids
minor planets, asteroids: general
minor planets, asteroids: individual: . . .
Moon
Oort Cloud
planets and satellites: atmospheres
planets and satellites: aurorae
planets and satellites: composition
planets and satellites: detection
planets and satellites: dynamical evolution and stability
planets and satellites: formation
planets and satellites: fundamental parameters
planets and satellites: gaseous planets
planets and satellites: general

planets and satellites: individual: . . .
planets and satellites: interiors
planets and satellites: magnetic fields
planets and satellites: oceans
planets and satellites: physical evolution
planets and satellites: rings
planets and satellites: surfaces
planets and satellites: tectonics
planets and satellites: terrestrial planets
planet–disc interactions
planet–star interactions
protoplanetary discs
zodiacal dust

Stars
stars: abundances
stars: activity
stars: AGB and post-AGB
stars: atmospheres
(stars:) binaries *(including multiple)*: close
(stars:) binaries: eclipsing
(stars:) binaries: general
(stars:) binaries: spectroscopic
(stars:) binaries: symbiotic
(stars:) binaries: visual
stars: black holes
(stars:) blue stragglers
(stars:) brown dwarfs
stars: carbon
stars: chemically peculiar
stars: chromospheres
(stars:) circumstellar matter
stars: coronae
stars: distances
stars: dwarf novae
stars: early-type
stars: emission-line, Be
stars: evolution
stars: flare
stars: formation
stars: fundamental parameters
(stars:) gamma-ray burst: general
(stars:) **gamma-ray burst: individual: . . .**
stars: general
(stars:) Hertzsprung–Russell and colour–magnitude diagrams
stars: horizontal branch
stars: imaging
stars: individual: . . .
stars: interiors

stars: jets
stars: kinematics and dynamics
stars: late-type
stars: low-mass
stars: luminosity function, mass function
stars: magnetars
stars: magnetic field
stars: massive
stars: mass-loss
stars: neutron
(stars:) novae, cataclysmic variables
stars: oscillations *(including pulsations)*
stars: peculiar *(except chemically peculiar)*
(stars:) planetary systems
stars: Population II
stars: Population III
stars: pre-main-sequence
stars: protostars
(stars:) pulsars: general
(stars:) **pulsars: individual: . . .**
stars: rotation
stars: solar-type
(stars:) starspots
stars: statistics
(stars:) subdwarfs
(stars:) supergiants
(stars:) supernovae: general
(stars:) **supernovae: individual: . . .**
stars: variables: Cepheids
stars: variables: Scuti
stars: variables: general
stars: variables: RR Lyrae
stars: variables: S Doradus
stars: variables: T Tauri, Herbig Ae/Be
(stars:) white dwarfs
stars: winds, outflows
stars: Wolf–Rayet

Interstellar medium (ISM), nebulae
ISM: abundances
ISM: atoms
ISM: bubbles
ISM: clouds
(ISM:) cosmic rays
(ISM:) dust, extinction
ISM: evolution
ISM: general
(ISM:) HII regions
(ISM:) Herbig–Haro objects

ISM: individual objects: . . .
(except planetary nebulae)
ISM: jets and outflows
ISM: kinematics and dynamics
ISM: lines and bands
ISM: magnetic fields
ISM: molecules
(ISM:) photodissociation region (PDR)
(ISM:) planetary nebulae: general
(ISM:) **planetary nebulae: individual: . . .**
ISM: structure
ISM: supernova remnants

The Galaxy
Galaxy: abundances
Galaxy: bulge
Galaxy: centre
Galaxy: disc
Galaxy: evolution
Galaxy: formation
Galaxy: fundamental parameters
Galaxy: general
(Galaxy:) globular clusters: general
(Galaxy:) **globular clusters: individual: . . .**
Galaxy: halo
Galaxy: kinematics and dynamics
(Galaxy:) local interstellar matter
Galaxy: nucleus
(Galaxy:) open clusters and associations: general
(Galaxy:) **open clusters and associations: individual: . . .**
(Galaxy:) solar neighbourhood
Galaxy: stellar content
Galaxy: structure

Galaxies
galaxies: abundances
galaxies: active
galaxies: bar
(galaxies:) BL Lacertae objects: general
(galaxies:) **BL Lacertae objects: individual: . . .**
galaxies: bulges
galaxies: clusters: general

galaxies: clusters: individual: . . .
galaxies: clusters: intracluster medium
galaxies: disc
galaxies: distances and redshifts
galaxies: dwarf
galaxies: elliptical and lenticular, cD
galaxies: evolution
galaxies: formation
galaxies: fundamental parameters
galaxies: general
galaxies: groups: general

galaxies: groups: individual: . . .
galaxies: haloes
galaxies: high-redshift

galaxies: individual: . . .
galaxies: interactions
(galaxies:) intergalactic medium
galaxies: irregular
galaxies: ISM
galaxies: jets
galaxies: kinematics and dynamics
(galaxies:) Local Group
galaxies: luminosity function, mass function
(galaxies:) Magellanic Clouds
galaxies: magnetic fields
galaxies: nuclei
galaxies: peculiar
galaxies: photometry
(galaxies:) quasars: absorption lines
(galaxies:) quasars: emission lines
(galaxies:) quasars: general

(galaxies:) **quasars: individual: . . .**
(galaxies:) quasars: supermassive black holes
galaxies: Seyfert
galaxies: spiral
galaxies: starburst
galaxies: star clusters: general

galaxies: star clusters: individual: . . .
galaxies: star formation
galaxies: statistics
galaxies: stellar content
galaxies: structure

Cosmology
(cosmology:) cosmic background radiation
(cosmology:) cosmological parameters
(cosmology:) dark ages, reionization, first stars
(cosmology:) dark energy
(cosmology:) dark matter
(cosmology:) diffuse radiation
(cosmology:) distance scale
(cosmology:) early Universe
(cosmology:) inflation
(cosmology:) large-scale structure of Universe
cosmology: miscellaneous
cosmology: observations
(cosmology:) primordial nucleosynthesis
cosmology: theory

Resolved and unresolved sources as a function of wavelength
gamma-rays: diffuse background
gamma-rays: galaxies
gamma-rays: galaxies: clusters
gamma-rays: general
gamma-rays: ISM
gamma-rays: stars
infrared: diffuse background
infrared: galaxies
infrared: general
infrared: ISM
infrared: planetary systems
infrared: stars
radio continuum: galaxies
radio continuum: general
radio continuum: ISM
radio continuum: planetary systems
radio continuum: stars
radio continuum: transients
radio lines: galaxies
radio lines: general
radio lines: ISM
radio lines: planetary systems
radio lines: stars
submillimetre: diffuse background
submillimetre: galaxies
submillimetre: general
submillimetre: ISM
submillimetre: planetary systems
submillimetre: stars
ultraviolet: galaxies
ultraviolet: general
ultraviolet: ISM
ultraviolet: planetary systems
ultraviolet: stars
X-rays: binaries
X-rays: bursts
X-rays: diffuse background
X-rays: galaxies
X-rays: galaxies: clusters
X-rays: general
X-rays: individual: . . .
X-rays: ISM
X-rays: stars

Transients
(transients:) black hole mergers
(transients:) black hole - neutron star mergers
(transients:) fast radio bursts
(transients:) gamma-ray bursts
(transients:) neutron star mergers
transients: novae
transients: supernovae
transients: tidal disruption events